

Cobalt Phosphide Double-Shelled Nanocages: Broadband Light-Harvesting Nanostructures for Efficient Photothermal Therapy and Self-Powered Photoelectrochemical Biosensing

Jingqi Tian, Houjuan Zhu, Jie Chen, Xinting Zheng, Hongwei Duan, Kanyi Pu,
and Peng Chen*

Ultra-broadband light-absorbing materials are highly desired for effective solar-energy harvesting. Herein, novel cobalt phosphide double-shelled nanocages (CoP-NCs) are synthesized. Uniquely, these CoP-NCs are able to nonselectively absorb light spanning the full solar spectrum, benefiting from its electronic properties and hollow nanostructure. They promise a wide range of applications involving solar energy utilization. As proof-of-concept demonstrations, CoP-NCs are employed here as effective photothermal agents to ablate cancer cells by utilizing their ability of near-infrared heat conversion, and as photoactive material for self-powered photoelectrochemical sensing by taking advantage of their ability of photon-to-electricity conversion.

Effectively harvesting solar energy for the production of other energy forms (e.g., electrical, chemical, thermal energy) through photovoltaic, photocatalytic, and photothermal routes is largely restrained by the narrow absorption window of the commonly used light-absorbing materials. In the solar spectrum, ultraviolet (UV, <400 nm), visible (400–760 nm), and infrared (IR, 760–3000 nm) lights constitute 6.8%, 38.9%, and 54.3% of the total solar energy,^[1] respectively. Although of utmost importance for solar energy conversion, materials for efficient broadband absorption expanding from UV to IR are currently rare.^[2]

Plasmonic metal nanoparticles have been devised to enhance the light absorption efficiency, but only within a

limited bandwidth centered at the plasmonic resonance wavelength of the nanoparticles.^[3] Although ordered assembly of plasmonic metal nanoparticles^[4a] or nanofabricated plasmonic structures^[4b] can greatly extend the absorption range, the preparations are often challenging and tedious, and the application scope is restricted by the particular structures. In addition, these plasmonic materials cannot be effectively used alone for photovoltaic and photocatalytic applications due to the short lifetime of photoinduced charge separation in metals.^[5]

Therefore, broadband light-absorbing semiconductor nanoparticles are highly desired. It has been demonstrated that introducing disorders on the surface of TiO₂ nanocrystals through hydrogenation at 200 °C for 5 d reduces its bandgap and thus extends its absorption to IR region.^[6] But the preparation process is tedious and the nanoparticles are not able to absorb beyond 1200 nm. In comparison to metal oxide nanoparticles, metal chalcogenide quantum dots can absorb lights in a wider window,^[7] arising from a narrower and tunable band gap,^[7a] localized surface plasmon resonances,^[7b] impurity-level transitions,^[7c] etc. But the applications of metal chalcogenides are largely limited by the serious photo-corrosion problem.

Recently, transition metal phosphide (TMP) nanostructures (nanowires, nanoplates, nanoparticles) have attracted

Dr. J. Tian, Dr. H. Zhu, J. Chen, Prof. H. Duan,
Prof. K. Pu, Prof. P. Chen
School of Chemical and Biomedical Engineering
Nanyang Technological University
637457, Singapore
E-mail: chenpeng@ntu.edu.sg

Dr. X. Zheng
Institute of Materials Research and Engineering
A*STAR (Agency for Science Technology and Research)
138634, Singapore



DOI: 10.1002/sml.201700798

considerable attention as photocatalysts because of their higher stability as compared to metal chalcogenides, and better conductivity as compared to metal oxides.^[8] The broadband-absorbing TMP nanostructures, however, have not yet been realized. We conceive that the absorption range and efficiency of TMPs may be greatly improved through intricate structure and morphology design.

In this contribution, a novel TMP nanostructure, cobalt phosphide double-shelled hollow nanocage (CoP-NC), was synthesized via low-temperature phosphidation from Prussian-blue-derived cobalt-oxide nanocage. Impressively, CoP-NCs are able to evenly absorb lights in an ultrawide range (without any decay up to 2500 nm, which is our measurement limit). Such a broadband absorber promises a wide spectrum of applications. As the proof-of-concept demonstrations, CoP-NCs were employed here as effective photo-thermal agents to ablate cancer cells by utilizing their ability of near infrared (NIR)-heat conversion, and as photoactive material for self-powered photoelectrochemical sensing by taking advantages of their ability of photon-to-electricity conversion.

The synthesis of cobalt phosphide double-shelled nanocages (CoP-NCs) is schematically illustrated in **Figure 1**. First, a cobalt Prussian-blue analogue (PBA) was synthesized by simply mixing $K_3[Co(CN)_6]$ and $Co(CH_3COO)_2 \cdot 4H_2O$ solution in the presence of polyvinylpyrrolidone, as previously reported.^[9] This is confirmed by X-ray diffraction (XRD) spectrum, in which the diffraction peaks can be perfectly ascribed to cubic phase of $Co_3[Co(CN)_6]_2 \cdot nH_2O$ (JCPDS No. 77–1161, Figure S1A, Supporting Information).^[10] Scanning electron microscopy (SEM) reveals that the obtained products are solid nanocubes (PBA-NCs) with a uniform size of ≈ 120 nm (**Figure 2A**). Further transmission electron microscopy (TEM) characterization shows that PBA-NCs are solid with smooth surface (**Figure 2C**).

Annealing at 450 °C, PBA-NCs were then converted into spinel Co_3O_4 as confirmed by XRD characterization (matching JCPDS No. 42–1467, Figure S1B, Supporting Information).^[9] The original solid nanocubes are transformed into hollow nanocages with a slightly decreased size (≈ 100 nm) and rougher surfaces (**Figure 2B,D**). High-resolution TEM (HRTEM) further reveals that the obtained Co_3O_4 nanocages (Co_3O_4 -NCs) exhibit the lattice fringes with interplane spacing of 0.286 and 0.247 nm corresponding to the (220) and (311) planes of Co_3O_4 (**Figure 2E**).^[11]

Subsequent phosphidation of Co_3O_4 -NCs under Ar atmosphere at 320 °C with NaH_2PO_2 as the phosphorus source led to disappearance of the Co_3O_4 peaks and appearance of the sharp characteristic diffraction peaks of orthorhombic CoP in XRD pattern (JCPDS No. 29–0497),^[10] indicating the complete phosphidation and high crystallinity (**Figure 2F**). SEM image shows that such low-temperature phosphidation reaction preserves the cage-like morphology (**Figure 2G**). Interestingly, TEM images indicate that, originated from the single-shelled (≈ 20 nm thickness) Co_3O_4 -NCs, the obtained CoP-NCs become a double-shelled hollow structure with shell thickness of ≈ 8 nm (**Figure 2H,I**). HRTEM images taken from the outer and inner shells of a CoP-NC show well-resolved lattice fringes with interplanar distances of 0.284 and 0.245 nm indexed to the (011) and (102) planes of CoP (**Figure 2J,K**).

Brunauer–Emmett–Teller (BET) characterization based on nitrogen adsorption/desorption suggests that CoP-NCs are nanoporous with a large specific surface area of $30.8 \text{ m}^2 \text{ g}^{-1}$ (**Figure S2**, Supporting Information). Presumably, the small pores (<10 nm) indicated by BET measurement are on the cage shells, while the indicated larger pores (10–100 nm) are actually gaps between double shells, hollow core of the particle, and interspace between individual particles. For comparison purpose, we also synthesized CoP nanoparticles (CoP-NPs) simply by annealing the mixture of $Co(CH_3COO)_2 \cdot 4H_2O$ and NaH_2PO_2 at 350 °C in Ar atmosphere. The synthesis is verified by XRD characterization and TEM, which shows that the obtained CoP-NPs are solid nanoparticles <100 nm (**Figure S3**, Supporting Information). In comparison to CoP-NCs, CoP-NPs are not porous and thus has a small specific surface area of $3.9 \text{ m}^2 \text{ g}^{-1}$ (**Figure S2**, Supporting Information).

We propose that the formation of double-shelled CoP nanocages from Co_3O_4 nanocages is attributable to the Kirkendall effect (**Figure 1**).^[12] Specifically, PH_3 released from NaH_2PO_2 ^[13] can penetrate into the nanoporous Co_3O_4 -NCs, leading to the simultaneous formation of CoP layers from both exterior and interior sides. But the outward diffusion of cobalt ions is faster than the inward diffusion of phosphorus ions. As a consequence, the original Co_3O_4 shell is separated into two thinner CoP shells. In agreement with this notion, the thickness of Co_3O_4 shell (≈ 20 nm) is indeed approximately two times of that of CoP shell (≈ 8 nm) as shown by TEM characterization (**Figure 2D,I**).

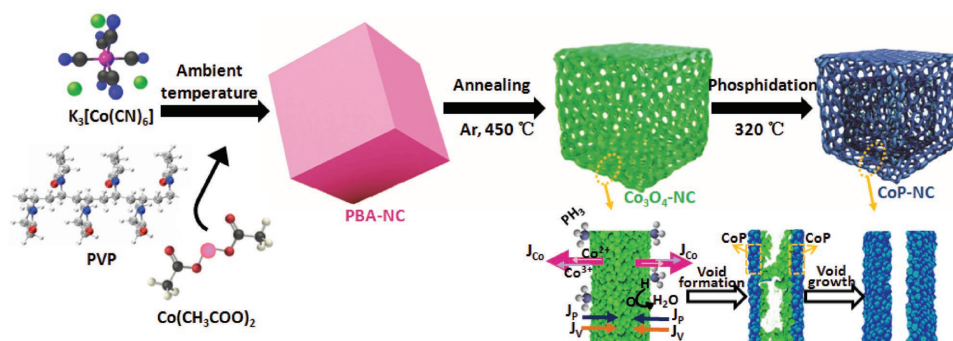


Figure 1. Schematic of the synthesis route of double-shelled CoP nanocages.

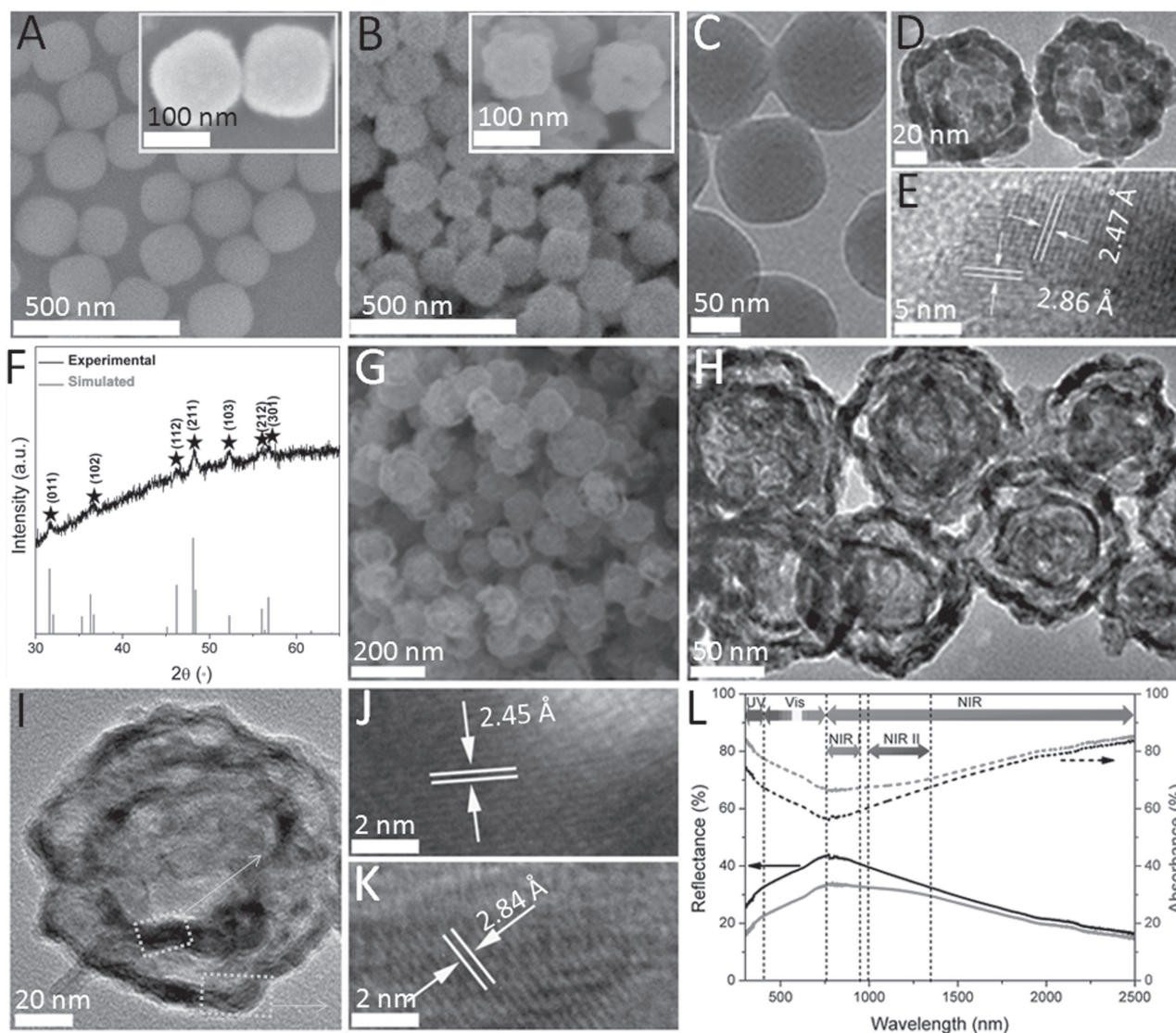


Figure 2. SEM images of A) PBA nanocubes and B) Co₃O₄ nanocages. TEM images of C) PBA nanocubes and D,E) Co₃O₄ nanocages. F) XRD pattern of CoP nanocages. G) SEM image and H,I) TEM images of CoP nanocages. J,K) Zoom-in high-resolution TEM images of the two highlighted areas in (I). L) Diffuse reflectance spectra of CoP nanocages and CoP nanoparticles.

As expected, X-ray photoelectron spectroscopy (XPS) reveals the presence of Co, P, and O elements in CoP-NCs at the ratio of 1.13:1:0.06 (Figure S4A, Supporting Information). The characteristic peaks of Co 2p_{3/2} (779.3 eV) and P 2p_{3/2} (129.8 eV) in the high-resolution XPS spectra confirm the identity of CoP (Figure S4B,C, Supporting Information).^[13] The binding energy of Co 2p_{3/2} is higher than that of metallic Co (778.4 eV) and the binding energy of P 2p_{3/2} is lower than that of elemental P (130.2 eV).^[14] These observations suggest that Co in CoP has a partial positive charge (δ^+) and P has a partial negative charge (δ^-). Such small transfer of electron density from Co to P has also been reported in other metal phosphides.^[15] The Co–O (781.7 eV) and P–O (134.0 eV) peaks in the XPS spectra are due to surface oxidation of CoP nanocages in ambient.^[16]

The diffuse reflectance spectrum of CoP-NCs is obtained in the wavelength range of 300–2500 nm (Figure 2L). Interestingly and uniquely, CoP-NCs exhibit uniform strong

absorption (average $\approx 5\%$) in such wide spectral range. Conceivably, the ultrawide range of light absorption may be attributed to the following electronic transitions: 1) band-to-band transition from the valence band (originated from Co 3d hybridization with P 3p orbitals) to the conduction band (originated from Co 4s hybridization with P 4s orbitals), which induces the absorption below 750 nm, consistent with the measured band gap of CoP-NCs (1.65 eV; Figure S5, Supporting Information); 2) metal–ligand charge transfer from Co 3d to P 4s orbitals, which also underlies the absorption in UV–vis region;^[17] 3) d–d transition of Co, which accounts for the absorption in the visible and NIR region;^[18] 4) intraband transition owing to free charge carrier absorption, which accounts for the absorption in the NIR region.^[19] In addition to the electronic structures, the optical absorption is also influenced by the nanoarchitecture of the material. As shown in Figure 2L, the total absorption of double-shelled hollow CoP-NCs is higher than the solid CoP-NPs (75% vs 69%).

As proposed by a number of studies, such absorption enhancement may be attributable to the multiple reflections of light within the cavity of the nanocage.^[20] Additionally, it may also be contributed by Rayleigh scattering that occurs when the void size in a nanostructure is much smaller than the wavelength of light.^[20b]

The photothermal therapy relies on effective agents that can convert light energy into heat for cancer-cell killing. The biological transparency windows located in 650–950 nm (first NIR window) and 1000–1350 nm (second NIR window) allow for deep tissue penetration and minimal tissue absorption and scattering.^[21] Therefore, those photothermal agents that can efficiently absorb NIR (particularly in the second window) are desirable. Although various organic and inorganic photothermal agents working in the first NIR window have been devised,^[22] nanoabsorbers effectively responsive to the second window are still rare.^[23] Uniquely, our CoP-NCs work in both windows. The extinction spectrum of CoP-NCs aqueous solution indicates the broad absorption covering the entire UV–vis–NIR range (Figure S6, Supporting Information). Noteworthy, the extinction coefficient of the CoP-NC at 808 nm is calculated to be $5.65 \times 10^{-11} \text{ cm}^2$, which is larger than that of gold nanorods ($4.5 \times 10^{-11} \text{ cm}^2$),^[24a] CuSe QDs ($2.9 \times 10^{-13} \text{ cm}^2$),^[24b] indicating the superior light harvesting ability of CoP-NCs. The ultrabroad absorption spectrum of CoP-NCs allows not only the flexibility to work with different light sources available, but also, more importantly, the possibility of using a lower energy broadband light source (instead of commonly a strong single wavelength laser) to minimize the lateral tissue damage.

The as-synthesized CoP-NCs were further functionalized with polyethylene glycol (PEG) to improve their biocompatibility. The PEG modified CoP-NCs (PEG-CoP-NCs), which can stably disperse in aqueous solutions, exhibit a larger hydrodynamic size ($\approx 160 \text{ nm}$) than that of bare CoP-NCs ($\approx 100 \text{ nm}$), confirming the coating of a PEG layer (Figure S7, Supporting Information). The successful functionalization of PEG is also evidenced by the appearance of characteristic peaks in the Fourier transform infrared (FTIR) spectra from PEG (Figure S8, Supporting Information), specifically, peaks at 2868 cm^{-1} corresponding to $-\text{CH}_2$ in alkyl chains, 1062 cm^{-1} due to vibration of $-\text{C}-\text{O}-\text{C}$, 1342 and 1465 cm^{-1} originated from $\text{C}-\text{H}$ groups, 1651 cm^{-1} from $\text{C}-\text{OH}$ groups, respectively.^[25] The aqueous suspension of PEG-CoP-NCs retains the broadband absorption profile (Figure S9, Supporting Information).

As demonstrated in Figure 3A, the temperature of the aqueous suspension of PEG-CoP-NCs quickly escalated in a concentration-dependent manner under irradiation of an 808 nm NIR laser (0.8 W cm^{-2}). More specifically, with the PEG-CoP-NCs concentration at 0.2 mg mL^{-1} , a large temperature increase (ΔT) of $51.5 \text{ }^\circ\text{C}$ was attained within 8 min. These results indicate that CoP-NCs are able to convert NIR energy into thermal energy rapidly and efficiently. Furthermore, excellent reversibility and cycling stability were also observed (Figure 3C). The photothermal conversion efficiency is calculated to be 28.2% (Figure S10A, Supporting Information), which is higher than that of commercial gold nanorods (21%),^[22a] $\text{Cu}_2\text{-xSe}$ nanocrystals (22%),^[22a] Cu_3S_5

nanocrystals (25.7%);^[22b] and comparable to Bi_2S_3 nanorods (28.1%),^[22d] and WO_{3-x} nanostructures (28.1%),^[22e] The photothermal conversion efficiency of solid PEG-CoP-NCs (23.6%) is inferior to PEG-CoP-NCs (Figure 3C: Figure S10B, Supporting Information) because the double-shelled hollow structure of CoP-NC can better absorb light due to internal reflection (Figure 2L) and allow water penetration for intimate thermal exchange. Moreover, PEG-CoP-NCs can also serve as an infrared thermal imaging contrast agent for in vivo bioimaging (Figure 3D). According to Alamar Blue viability assay (Figure 3E,F) and fluorescence confocal imaging of live/dead cell double staining (Figure 3G), PEG-CoP-NCs are essentially biocompatible whereas exhibiting high phototoxicity upon 808 nm NIR irradiation.

Noteworthy, CoP-NCs also have strong absorption in the second NIR window (Figure 2L), permitting photothermal therapy with even deeper tissue penetration. Under NIR irradiation at 1064 nm (0.8 W cm^{-2}), a temperature increase (ΔT) of $29.1 \text{ }^\circ\text{C}$ was reached within 8 min in the presence of 0.2 mg mL^{-1} PEG-CoP-NCs, which is sufficient to largely ablate cancer cells (Figure S11, Supporting Information). However, such a temperature rise is lower than that caused by 808 nm irradiation because of lower absorption (Figure S6, Supporting Information) and lower photothermal conversion efficiency ($\approx 21.2\%$) at 1064 nm . Taken together, PEG-CoP-NCs, which are able to utilize an ultrawide range of NIR, are promising photothermal agents for deep tissue cancer therapy.

Many solar-energy harvesting applications require semiconducting light absorbing materials because effective separation of excited electron–hole pairs is needed. As a proof-of-concept demonstration, the semiconducting CoP-NCs were employed for photoelectrochemical (PEC) sensing of H_2O_2 and glucose. PEC sensors based on oxidation of H_2O_2 have been previously demonstrated.^[26a,b] But to avoid the interference from other physiological reductants (e.g., ascorbic acid), we constructed a $\text{Cu}_2\text{O}/\text{CoP-NCs}$ p–n heterojunction photocathode to detect H_2O_2 based on its reduction.

The sensing mechanism and the energy diagram of the photocathode are illustrated in Figure 4A. A p–n junction formed at the interface of p-type Cu_2O and n-type CoP-NCs gives a favorable energy band alignment for photogenerated electrons to transport from the conduction band (CB) of Cu_2O to the CB of CoP-NCs and subsequently reduce H_2O_2 to H_2O ; and on the other hand the photogenerated holes transport from the valence band (VB) of the CoP-NCs to the VB of Cu_2O and finally reach the counter electrode for water oxidation. With glucose oxidase (GOD) modification, photogenerated electrons in the CB of CoP-NCs transfer further to GOD which has a moderately lower redox potential ($-97 \text{ mV vs NHE, pH} = 7.4$)^[27] below CB of CoP-NCs. This is evidenced by the observation that the photoresponse from the ITO/ $\text{Cu}_2\text{O}/\text{CoP-NCs}/\text{GOD}$ photocathode is larger than that from the ITO/ $\text{Cu}_2\text{O}/\text{CoP-NCs}$ photocathode (Figure S13, Supporting Information). By contrast, ITO/GOD electrode is not photoresponsive at all (Figure S14, Supporting Information) and ITO/ $\text{Cu}_2\text{O}/\text{GOD}$ electrode produces much smaller photoresponse (Figure S13, Supporting Information), indicating that GOD itself does not generate photocurrent

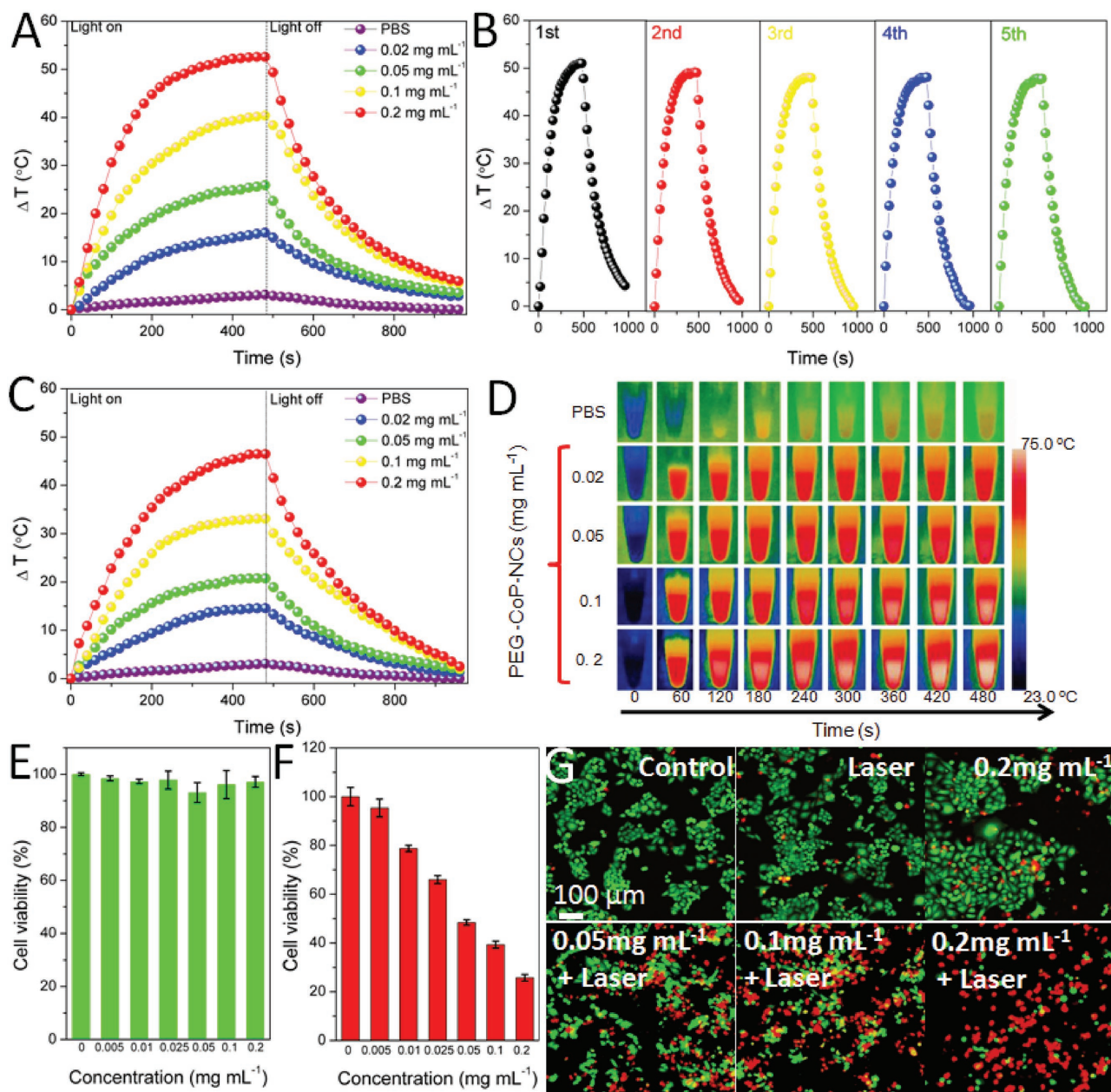


Figure 3. A) The photothermal profiles of PEG-CoP-NC dispersion at different concentrations in PBS buffer. B) The photothermal conversion cycling performance of PEG-CoP-NCs (0.2 mg mL⁻¹). C) The photothermal profiles of PEG-CoP-NP dispersion at different concentrations in PBS buffer. D) IR thermal images of PEG-CoP-NCs at various concentrations. E) Relative viabilities of HeLa cells after being incubated with various concentration of PEG-CoP-NCs for 24 h. F) Relative viabilities of HeLa cells after incubation with PEG-CoP-NCs at different concentrations. Error bars are the standard deviations obtained from three different samples. G) Confocal fluorescence images of HeLa cells after incubated with/without PEG-CoP-NCs of different concentrations. All experiments, except the experiment in (E), and the two control experiments (top-left and top-right) in (G), were conducted under 808 nm laser irradiation for 8 min, with a power density of 0.8 W cm⁻².

and CoP-NCs are important for transfer of the photogenerated electrons, thus photoresponse. The construction of the photocathode was characterized and verified as shown in Figure S12 (Supporting Information). To demonstrate the concept of light-driven self-powered sensing which may be promising for batteryless implantable devices, the following detection measurements were made without applying any voltage bias between the cathode and anode.

In response to light pulses, the ITO/Cu₂O/CoP-NC photocathode shows an enhanced current density as compared

with ITO/Cu₂O photocathode (0.13 vs 0.06 mA cm⁻²), demonstrating the significant improvement of the photoelectric conversion efficiency because of the incorporation of n-type CoP-NCs (Figure 4B). Introduction of H₂O₂ (10 × 10⁻⁶ M) leads to a further increase of photocurrent to 0.16 mA cm⁻². Under continuous illumination, the photocurrent increases with increasing concentration of H₂O₂ (Figure 4C). As shown, our PEC sensor exhibits two linear response ranges ((1–20) × 10⁻⁶ and (20–220) × 10⁻⁶ M) with the detection limit (LOD, at S/N = 3) of 100 × 10⁻⁹ M

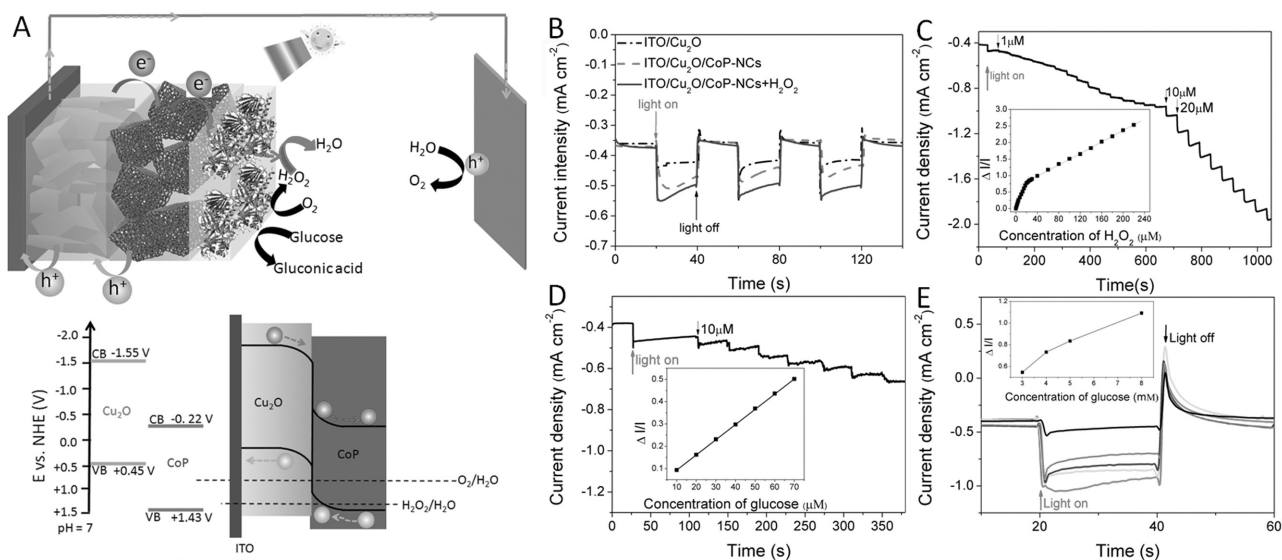


Figure 4. A) Schematic illustration of the light-driven self-powered photoelectrochemical biosensor for H_2O_2 or glucose detection, and the energy level diagram. The energy levels of Cu_2O were obtained from a previous report,^[28] and that of CoP-NCs were determined in Figure S5 (Supporting Information). B) Photoresponse of ITO/ Cu_2O photocathode in PBS (0.1 M, pH = 7.4), and ITO/ Cu_2O /CoP-NCs photocathode in 0.1 M PBS (pH = 7.4) with/without 10×10^{-6} M H_2O_2 . C) Typical photocurrent response of ITO/ Cu_2O /CoP-NCs photocathode to dropwise addition of H_2O_2 , with a bias potential of 0 V (vs Ag/AgCl). The inset is the corresponding dose–response curve. D) Typical photocurrent response of ITO/ Cu_2O /CoP-NCs/GOD photocathode to dropwise addition of glucose, with a bias potential of 0 V (vs Ag/AgCl). The inset is the corresponding dose–response curve. E) Photocurrent response of the ITO/ Cu_2O /CoP-NCs/GOD photocathode in the presence of different concentrations of glucose (from top to bottom: 3, 4, 6, and 8×10^{-3} M) at 0 V (vs Ag/AgCl) under simulated solar illumination.

(Figure 4C), which is superior to the PEC sensor with an ITO/ Cu_2O photocathode (Figure S15, Supporting Information) and other PEC sensors.^[26cc] The linear-sweep photovoltammograms (Figure S16, Supporting Information) for ITO/ Cu_2O /CoP-NCs with or without saturated N_2 in PBS containing 10×10^{-6} M H_2O_2 exhibit a similar photocurrent, indicating the measured reduction current is solely from H_2O_2 without interference from O_2 . Immobilization of GOD on a Cu_2O /CoP-NCs photocathode (ITO/ Cu_2O /CoP-NCs/GOD) endows it the ability to detect glucose because glucose oxidation specifically catalyzed by GOD produces H_2O_2 . As demonstrated in Figure 4D, the photocurrent of GOD-functionalized photocathode increases with glucose concentration, with an LOD of 2.6×10^{-6} M (S/N = 3), and it is highly selective toward glucose without obvious interference from other sugars (Figure S17, Supporting Information). Furthermore, Figure 4E shows that our PEC sensor responds well to the physiological glucose levels in a dose-dependent manner.

In summary, we report a unique broadband light-harvesting nanostructure, CoP double-shelled nanocage, for solar energy utilization. Such CoP-NCs is formed by a low-temperature phosphidation process accompanied with Kirkendall effect. The remarkable light absorbing ability covering the full solar spectrum is benefited from the unique electronic properties as well as the double-shelled hollow structure. As a proof-of-concept demonstration, CoP-NCs were employed here for photothermal therapy utilizing their ability of NIR-heat conversion and for light-driven, self-powered photoelectrochemical sensing, taking advantage of their ability of photoelectric conversion. We envision that CoP-NCs promise a wide range of applications, in addition to the herein demonstrated, such as photothermal seawater

desalination, photothermal catalysis or photocatalysis, and photovoltaic cells. We also anticipate the potential of other nanostructured transition-metal phosphides for solar-energy harvesting.

Supporting Information

Supporting Information is available from the Wiley Online Library or from the author.

Acknowledgements

This research was supported by an AcRF tier 2 grant (MOE2014-T2-1-003) from Ministry of Education (Singapore).

Conflict of Interest

The authors declare no conflict of interest.

- [1] J. Cui, Y. Li, L. Liu, L. Chen, J. Xu, J. Ma, G. Fang, E. Zhu, H. Wu, L. Zhao, L. Wang, Y. Huang, *Nano Lett.* **2015**, *15*, 6295.
- [2] a) W. Zou, C. Visser, J. A. Maduro, M. S. Pshenichnikov, J. C. Hummelen, *Nat. Photonics* **2012**, *6*, 560; b) Y. Zhang, Z. Sun, S. Cheng, F. Yan, *ChemSusChem* **2016**, *9*, 813.
- [3] H. A. Atwater, A. Polman, *Nat. Mater.* **2010**, *9*, 205.

- [4] a) L. Zhou, Y. Tan, J. Wang, W. Xu, Y. Yuan, W. Cai, S. Zhu, J. Zhu, *Nat. Photonics* **2016**, *10*, 393; b) J. Huang, C. Liu, Y. Zhu, S. Masala, E. Alarousu, Y. Han, A. Fratallocchi, *Nat. Nanotechnol.* **2015**, *11*, 60.
- [5] S. Linic, P. Christopher, D. B. Ingram, *Nat. Mater.* **2011**, *10*, 911.
- [6] X. Chen, L. Liu, P. Y. Yu, S. S. Mao, *Science* **2011**, *331*, 746.
- [7] a) S. V. Kershaw, A. S. Susha, A. L. Rogach, *Chem. Soc. Rev.* **2013**, *42*, 3033; b) J. M. Luther, P. K. Jain, T. Ewers, A. P. Alivisatos, *Nat. Mater.* **2011**, *10*, 361; c) A. Stavrinadis, G. Konstantatos, *ChemPhysChem* **2016**, *17*, 632; d) X. Wang, G. Sun, N. Li, P. Chen, *Chem. Soc. Rev.* **2016**, *45*, 2239.
- [8] a) A. Dutta, S. K. Dutta, S. K. Mehetor, I. Mondal, U. Pal, N. Pradhan, *Chem. Mater.* **2016**, *28*, 1872; b) Z. Sun, Q. Yue, J. Li, J. Xu, H. Zheng, P. Du, *J. Mater. Chem. A* **2015**, *3*, 10243; c) S. Yi, J. Yan, B. Wulan, S. Li, K. Liu, Q. Jiang, *Appl. Catal., B* **2017**, *200*, 477; d) J. Tian, N. Cheng, Q. Liu, W. Xing, X. Sun, *Angew. Chem., Int. Ed.* **2015**, *54*, 5493.
- [9] N. Yan, L. Hu, Y. Li, Y. Wang, H. Zhong, X. Hu, X. Kong, Q. Chen, *J. Phys. Chem. C* **2012**, *116*, 7227.
- [10] a) J. Tian, Q. Liu, A. M. Asiri, X. Sun, *J. Am. Chem. Soc.* **2014**, *136*, 7587; b) Y. Li, M. A. Malik, P. O'Brien, *J. Am. Chem. Soc.* **2005**, *127*, 16020.
- [11] Y. Lin, H. Ji, Z. Shen, Q. Jia, D. Wang, *J. Mater. Sci.: Mater. Electron.* **2016**, *27*, 2086.
- [12] a) Y. Yin, R. M. Rioux, C. K. Erdonmez, S. Hughes, G. A. Somorjai, A. P. Alivisatos, *Science* **2004**, *304*, 711; b) R.-K. Chiang, R.-T. Chiang, *Inorg. Chem.* **2007**, *46*, 369.
- [13] A. P. Grosvenor, S. D. Wik, R. G. Cavell, A. Mar, *Inorg. Chem.* **2005**, *44*, 8988.
- [14] M. P. Seah, *Practical Surface Analysis: By Auger and X-Ray Photoelectron Spectroscopy* (Eds: D. Briggs, M. P. Seah), Wiley, New York **1983**.
- [15] A. W. Burns, K. A. Layman, D. H. Bale, M. E. Bussell, *Appl. Catal., A* **2008**, *343*, 68.
- [16] H. Li, P. Yang, D. Chu, H. Li, *Appl. Catal., A* **2007**, *325*, 34.
- [17] H. Zheng, *Phys. B* **1995**, *212*, 125.
- [18] a) N. Mironova, V. Skvortsova, U. Ulmanis, *Solid State Commun.* **1994**, *91*, 731; b) A. F. Lima, *J. Phys. Chem. Solids* **2014**, *75*, 148.
- [19] T. Jiang, X. Li, M. Bujoli-Doeuff, E. Gautron, L. Cario, S. Jobic, R. Gautier, *Inorg. Chem.* **2016**, *55*, 7729.
- [20] a) J.-Y. Lee, M.-C. Tsai, P.-C. Chen, T.-T. Chen, K.-L. Chan, C.-Y. Lee, R.-K. Lee, *J. Phys. Chem. C* **2015**, *119*, 25754; b) H. Zhou, T. Fan, T. Han, X. Li, J. Ding, D. Zhang, Q. Guo, H. Ogawa, *Nanotechnology* **2009**, *20*, 085603.
- [21] T.-M. Liu, J. Conde, T. Lipiński, A. Bednarkiewicz, C.-C. Huang, *NPG Asia Mater.* **2016**, *8*, e295.
- [22] a) C. M. Hessel, V. P. Pattani, M. Rasch, M. G. Panthani, B. Koo, J. W. Tunnell, B. A. Korgel, *Nano Lett.* **2011**, *11*, 2560; b) Q. Tian, F. Jiang, R. Zou, Q. Liu, Z. Chen, M. Zhu, S. Yang, J. Wang, J. Wang, J. Hu, *ACS Nano* **2011**, *5*, 9761; c) L. Cheng, S. Shen, S. Shi, Y. Yi, X. Wang, G. Song, K. Yang, G. Liu, T. E. Barnhart, W. Cai, Z. Liu, *Adv. Funct. Mater.* **2016**, *26*, 2185; d) J. Liu, X. Zheng, L. Yan, L. Zhou, G. Tian, W. Yin, L. Wang, Y. Liu, Z. Hu, Z. Gu, C. Chen, Y. Zhao, *ACS Nano* **2015**, *9*, 696; e) B. Li, Y. Zhang, R. Zou, Q. Wang, B. Zhang, L. An, F. Yin, Y. Hua, J. Hu, *Dalton. Trans.* **2014**, *43*, 6244; f) L. Cheng, J. Liu, X. Gu, H. Gong, X. Shi, T. Liu, C. Wang, X. Wang, G. Liu, H. Xing, W. Bu, B. Sun, Z. Liu, *Adv. Mater.* **2014**, *26*, 1886.
- [23] a) Z.-C. Wu, W.-P. Li, C.-H. Luo, C.-H. Su, C.-S. Yeh, *Adv. Funct. Mater.* **2015**, *25*, 6527; b) P. Vijayaraghavan, C.-H. Liu, R. Vankayala, C.-S. Chiang, K. C. Hwang, *Adv. Mater.* **2014**, *26*, 6689.
- [24] a) L. Martinez Maestro, P. Haro-González, A. Sánchez-Iglesias, L. M. Liz-Marzán, J. A. García Sole, D. Jaque, *Langmuir* **2014**, *30*, 1650; b) C. M. Hessel, V. P. Pattani, M. Rasch, M. G. Panthani, B. Koo, J. W. Tunnell, B. A. Korgel, *Nano Lett.* **2011**, *11*, 2560.
- [25] a) B. Gupta, N. Kumar, K. Panda, S. Dash, A. K. Tyagi, *Sci. Rep.* **2016**, *6*, 18372; b) M. Gajendiran, S. M. J. Yousuf, V. Elangovanb, S. Balasubramanian, *J. Mater. Chem. B* **2014**, *2*, 418.
- [26] a) X. Zhang, L. Li, X. Peng, R. Chen, K. Huo, P. K. Chu, *Electrochim. Acta* **2013**, *108*, 491; b) H. Li, W. Hao, J. Hu, H. Wu, *Biosens. Bioelectron.* **2013**, *47*, 225; c) H. Zhang, Q. Gao, H. Li, *J. Solid State Electrochem.* **2016**, *20*, 1565; d) D. Chen, H. Zhang, X. Li, J. Li, *Anal. Chem.* **2010**, *82*, 2253; e) J. Zhang, L. Tu, S. Zhao, G. Liu, Y. Wang, Y. Wang, Z. Yue, *Biosens. Bioelectron.* **2015**, *67*, 296.
- [27] S. Vogt, M. Schneider, H. Schäfer-Eberwein, G. Nöll, *Anal. Chem.* **2014**, *86*, 7530.
- [28] A. Paracchino, J. C. Brauer, J.-E. Moser, E. Thimsen, M. Graetzel, *J. Phys. Chem. C* **2012**, *116*, 7341.

Received: March 10, 2017
Published online: